

A method to integrate and classify normal distributions

Abhranil Das^{*1,3} and Wilson S Geisler^{2,3}

¹Department of Physics, The University of Texas at Austin

²Department of Psychology, The University of Texas at Austin

³Center for Perceptual Systems, The University of Texas at Austin

July 18, 2021

Abstract

Univariate and multivariate normal probability distributions are widely used when modeling decisions under uncertainty. Computing the performance of such models requires integrating these distributions over specific domains, which can vary widely across models. Besides some special cases where these integrals are easy to calculate, there exists no general analytical expression, standard numerical method or software for these integrals. Here we present mathematical results and open-source software that provide (i) the probability in any domain of a normal in any dimensions with any parameters, (ii) the probability density, distribution, and percentage points of any function of a normal vector, (iii) the error matrix that measures classification performance amongst any number of normal distributions, and the optimal discriminability index, (iv) dimension reduction and visualizations for such problems, and (v) tests for how reliably these methods can be used on given data. We demonstrate these tools with vision research applications of detecting occluding objects in natural scenes, and detecting camouflage.

Keywords: multivariate normal, integration, classification, signal detection theory, Bayesian ideal observer, vision

1 Introduction

The univariate or multivariate normal (henceforth called simply ‘normal’) is arguably the most important and widely-used probability distribution. It is frequently used because various central-limit theorems guarantee that normal distributions will occur commonly in nature, and because it is the simplest and most tractable distribution that allows arbitrary correlations between the variables.

Normal distributions form the basis of many theories and models in the natural and social sciences. For example, they are the foundation of Bayesian statistical decision/classification theories using Gaussian discriminant analysis,¹ and are widely applied in diverse fields such as vision science, neuroscience, probabilistic planning in robotics, psychology, and economics. These theories specify optimal performance under uncertainty, and are often used to provide a benchmark against which to evaluate the performance (behavior) of humans, other animals, neural circuits

or algorithms. They also serve as a starting point in developing other models/theories that describe sub-optimal performance of agents.

To compute the performance predicted by such theories it is necessary to integrate the normal distributions over specific domains. For example, a particularly common task in vision science is classification into two categories (such as detection and discrimination tasks). The predicted maximum accuracy in such tasks is determined by integrating normals over domains defined by a quadratic decision boundary.^{2,3} Predicted accuracy of sub-optimal models is determined by integrating over other domains.

Except for some special cases where these integrals are easier to calculate^{4,5} (e.g. where two normals have equal covariance and the optimal classification boundary is flat), there exists no general analytical expression, numerical method or standard software tool to quickly and accurately integrate arbitrary normals over arbitrary domains, or to compute classification errors and the discriminability index d' . Evaluating these quantities thus frequently requires the limiting assumption of equal variance. This impedes the quick testing, comparison, and optimization of models. Here we describe a mathematical method and accompanying software implementation which provides functions to (i) integrate normals with arbitrary means and covariances in any number of dimensions over arbitrary domains, (ii) compute the pdf, cdf and inverse cdf of any function of a multinormal variable (normal vector), and (iii) compute the performance of classifying amongst any number of normals. This is available as a Matlab toolbox ‘Integrate and classify normal distributions’, and the source code is at github.com/abhranildas/IntClassNorm.

We first review and assimilate previous mathematical results into a method to integrate arbitrary normals over quadratic domains. Then we present our method to integrate them over any domain, and consequently to compute the distribution of any real-valued function of a normal vector. We describe how these results can be used to compute error rates (and other relevant quantities) for Bayes-optimal and custom classifiers, given arbitrary priors and outcome cost matrix. We then present some methods to reduce problems to fewer dimensions, for analysis or visualization. Next, we provide a way to test whether directly measured samples from the actual distributions in a classification problem are close enough to normal to trust the computations from the toolbox. After describing the methods and software toolbox with examples, we demonstrate their accuracy and

^{*}abhranil.das@utexas.edu

speed across a variety of problems, and then illustrate them with two applications from our laboratory: modeling detection of occluding targets in natural scenes, and detecting camouflage.

2 Integrating the normal

2.1 In quadratic domains: the generalized chi-square method

Integrating the normal in quadratic domains is important for optimally classifying them. The problem is the following: given a column vector $\mathbf{x} \sim N(\boldsymbol{\mu}, \boldsymbol{\Sigma})$, find the probability that

$$q(\mathbf{x}) = \mathbf{x}'\mathbf{Q}_2\mathbf{x} + \mathbf{q}_1'\mathbf{x} + q_0 > 0. \quad (1)$$

This can be conceptualized as the multi-dimensional integral of the normal probability over the domain $q(\mathbf{x}) > 0$ (the ‘normal probability picture’), or the single-dimensional integral of the probability of the scalar quadratic function $q(\mathbf{x})$ of a normal vector, beyond 0 (the ‘function probability picture’).

Note that $\mathbf{x} = \mathbf{S}\mathbf{z} + \boldsymbol{\mu}$, where \mathbf{z} is standard normal, and the symmetric square root $\mathbf{S} = \boldsymbol{\Sigma}^{\frac{1}{2}}$ may be regarded as the multi-dimensional sd, since it linearly scales the normal (like σ in 1d), and its eigenvectors and values are the axes of the 1 sd error ellipsoid. We first invert this transform to standardize the normal: $\mathbf{z} = \mathbf{S}^{-1}(\mathbf{x} - \boldsymbol{\mu})$. This decorrelates or whitens the variables, and transforms the integration domain to a different quadratic:

$$\begin{aligned} \tilde{q}(\mathbf{z}) &= \mathbf{z}'\tilde{\mathbf{Q}}_2\mathbf{z} + \tilde{\mathbf{q}}_1'\mathbf{z} + \tilde{q}_0 > 0, \text{ with} \\ \tilde{\mathbf{Q}}_2 &= \mathbf{S}\mathbf{Q}_2\mathbf{S}, \\ \tilde{\mathbf{q}}_1 &= 2\mathbf{S}\mathbf{Q}_2\boldsymbol{\mu} + \mathbf{S}\mathbf{q}_1, \\ \tilde{q}_0 &= q(\boldsymbol{\mu}). \end{aligned} \quad (2)$$

Now the problem is to find the probability of the standard normal \mathbf{z} in this domain. If there is no quadratic term $\tilde{\mathbf{Q}}_2$, $\tilde{q}(\mathbf{z})$ is normally distributed, the integration domain boundary is a flat, and the probability is $\Phi(\frac{\tilde{q}_0}{\|\tilde{\mathbf{q}}_1\|})$, where Φ is the standard normal cdf.⁴

Otherwise, say $\tilde{\mathbf{Q}}_2 = \mathbf{R}\mathbf{D}\mathbf{R}'$ is its eigen-decomposition, where \mathbf{R} is orthogonal, i.e. a roto-reflection. So $\mathbf{y} = \mathbf{R}'\mathbf{z}$ is also standard normal, and in this space the quadratic is:

$$\begin{aligned} \hat{q}(\mathbf{y}) &= \mathbf{y}'\mathbf{D}\mathbf{y} + \mathbf{b}'\mathbf{y} + \tilde{q}_0 \quad (\mathbf{b} = \mathbf{R}'\tilde{\mathbf{q}}_1) \\ &= \sum_i (D_i y_i^2 + b_i y_i) + \sum_{i'} b_{i'} y_{i'} + \tilde{q}_0 \\ &\quad (i \text{ and } i' \text{ index the nonzero and zero eigenvalues}) \\ &= \sum_i D_i \left(y_i + \frac{b_i}{2D_i} \right)^2 + \sum_{i'} b_{i'} y_{i'} + \tilde{q}_0 - \sum_i \left(\frac{b_i}{2D_i} \right)^2 \\ &= \sum_i D_i \chi_{1, (b_i/2D_i)^2}^2 + x, \end{aligned}$$

a weighted sum of non-central chi-square variables χ'^2 , each with 1 degree of freedom, and a normal variable $x \sim N(m, s)$. So this is a generalized chi-square variable $\tilde{\chi}_{\mathbf{w}, \mathbf{k}, \boldsymbol{\lambda}, m, s}^2$, where we merge the non-central chi-squares with the same weights, so that the vector of their weights \mathbf{w} are the *unique* nonzero eigenvalues among D_i , their degrees of freedom \mathbf{k} are the numbers of times

the eigenvalues occur, and their non-centralities, and normal parameters are:

$$\lambda_j = \frac{1}{4w_j^2} \sum_{i: D_i = w_j} b_i^2, \quad m = q(\boldsymbol{\mu}) - \mathbf{w} \cdot \boldsymbol{\lambda}, \quad s = \sqrt{\sum_{i'} b_{i'}^2}.$$

The required probability, $p(\tilde{\chi}^2 > 0)$, is now a 1d integral, computable using, say, Ruben’s⁶ or Davies’⁷ methods.

We note that to the best of our knowledge, this complete general theory has not been described in the previous literature. Compared to previous software that implements specific forms of this theory for particular quadratics such as ellipsoids,⁵ this method correctly handles all quadratics (ellipsoids, hyperboloids, paraboloids and degenerate conics) in all dimensions.

2.2 In any domain: the ray-scan method

Since the normal distribution tails off infinitely outwards, it is inefficient to numerically integrate it over a finite uniform Cartesian grid, which would be large and collect ever-reducing masses outwards, yet omit some mass where it is truncated. Also, if the normal is elongated by unequal variances and strong covariances, or the integration domain is complex and non-contiguous, naïve integration grids will waste resources in regions or directions with low density. One then needs to visually inspect and arduously hand-tailor the integration grid to fit the problem shape.

Our method, presented below, standardizes the normal to symmetrize it, then divides the integration into polar coordinates that match this symmetry. The radial integral is calculated analytically, so it collects the entire mass to infinity without omission, machine imprecision, or using computation resources. The remaining integral is over a angular grid that is finite, so it can be done efficiently. The method is thus fast and accurate to arbitrary tolerance for all problem shapes without needing any manual adjustment.

2.2.1 Standard polar form

The problem is to find the probability that some general $f(\mathbf{x}) > 0$. As before, we first standardize the space to obtain $\tilde{f}(\mathbf{z}) = f(\mathbf{S}\mathbf{z} + \boldsymbol{\mu})$. Then we switch to polar axis-angle coordinates z and $\hat{\mathbf{n}}$: any point $\mathbf{z} = z\hat{\mathbf{n}}$, where the unit vector $\hat{\mathbf{n}}$ denotes the angle of that point, and z is its coordinate along the axis in this direction. Then the integral can be written as:

$$\int_{\tilde{\Omega}} (2\pi)^{-\frac{d}{2}} e^{-\frac{z^2}{2}} dz = \int_{\hat{\mathbf{n}}} d\hat{\mathbf{n}} \underbrace{\int_{\tilde{\Omega}_{\hat{\mathbf{n}}}} (2\pi)^{-\frac{d}{2}} e^{-\frac{z^2}{2}} dz}_{\text{axial integral}}.$$

where $\tilde{\Omega}$ is the domain where $\tilde{f}(\mathbf{z}) > 0$, and $\tilde{\Omega}_{\hat{\mathbf{n}}}$ is its slice along the axis $\hat{\mathbf{n}}$, i.e. where $\tilde{f}_{\hat{\mathbf{n}}}(z) = \tilde{f}(z\hat{\mathbf{n}}) > 0$. This may be called the ‘standard polar form’ of the integral. $d\hat{\mathbf{n}}$ is the differential angle element ($d\theta$ in 2d, $\sin \theta d\theta d\phi$ in 3d etc).

2.2.2 Integration domain on a ray

First let us consider the axial integration at direction $\hat{\mathbf{n}}$. Imagine that we ‘scan’ the integration domain with a ‘ray’ at this direction (arrow in fig. 1a), to determine the part of the ray that is in the

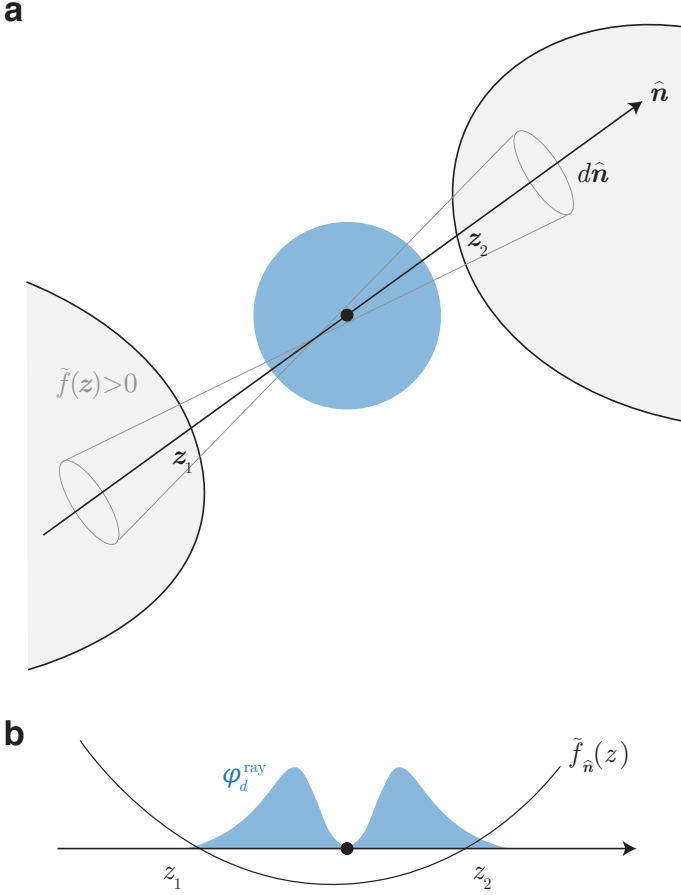


Figure 1: Method schematic. **a.** Standard normal error ellipse is blue. Arrow indicates a ray from it at angle \hat{n} in an angular slice $d\hat{n}$, crossing the gray standardized integration domain $\tilde{f}(z) > 0$ at z_1 and z_2 . **b.** 1d slice of this picture along the ray. The standard normal density along a ray is blue. $\tilde{f}_{\hat{n}}(z)$ is the slice of $\tilde{f}(z)$, crossing at z_1 and z_2 .

integration domain, defined by $\tilde{f}_{\hat{n}}(z) = \tilde{f}(z\hat{n}) > 0$. For example, if the integration domain is a quadratic such as eq. 2, its slice by the ray is given by:

$$\begin{aligned}\tilde{q}_{\hat{n}}(z) &= \tilde{q}(z\hat{n}) = \hat{n}'\tilde{\mathbf{Q}}_2\hat{n}z^2 + \tilde{\mathbf{q}}_1'\hat{n}z + \tilde{q}_0 \\ &= \tilde{q}_2(\hat{n})z^2 + \tilde{q}_1(\hat{n})z + \tilde{q}_0 > 0.\end{aligned}$$

This is a scalar quadratic domain in z that varies with the direction. Fig. 1b is an example of such a domain, where the integration domain is below z_1 (which is negative), and above z_2 .

Note that a sufficient description of the axial domain is to specify whether the ray begins inside the domain, and all the points at which it crosses the domain (so for a quadratic, its overall scale magnitude does not matter). We denote the first by the initial sign $\sigma(\hat{n}) = \text{sign}(\tilde{f}_{\hat{n}}(-\infty)) = 1/-1/0$ if the ray begins inside/outside/grazing the integration domain. For a quadratic domain, for example:

$$\sigma(\hat{n}) = \text{sign}(\tilde{q}_{\hat{n}}(-\infty)) = \begin{cases} \text{sign}(\tilde{q}_2(\hat{n})), & \text{if } \tilde{q}_2(\hat{n}) \neq 0, \\ -\text{sign}(\tilde{q}_1(\hat{n})), & \text{if } \tilde{q}_2(\hat{n}) = 0, \\ \text{sign}(\tilde{q}_0), & \text{if } \tilde{q}_2(\hat{n}) = \tilde{q}_1(\hat{n}) = 0. \end{cases}$$

The crossing points are the zeros $z_i(\hat{n})$ of $\tilde{f}_{\hat{n}}(z) = f(z\mathbf{S}\hat{n} + \mu)$ ($z_i\hat{n}$ are then the boundary points in the full space). For a

quadratic domain $\tilde{q}_{\hat{n}}(z)$ these are simply its roots. For a general domain, the zeros are harder to compute. Chebyshev polynomial approximations⁸ aim to find all zeros of a general function, but can be slow. Other numerical algorithms can find all function zeros in an interval to arbitrary accuracy. We use such an algorithm to find the zeros of $\tilde{f}_{\hat{n}}(z)$ within $(-m, m)$. This amounts to ray-scanning $f(x)$ within a Mahalanobis distance m of the normal. The error in the integral due to this approximation is therefore $< 2\bar{\Phi}(m)$.

In fig. 1, the initial sign along the ray is 1, and z_1 and z_2 are the crossing points.

Most generally, this method can integrate in any domain for which we can return its ‘scan’ (i.e. the initial sign and crossing points) along any ray \hat{n} from any origin \mathbf{o} . So if a domain is already supplied in this ‘ray-scan’ function form $f_{\text{ray}} : \mathbf{o}, \hat{n} \rightarrow (\sigma, z_i)$, our method can readily integrate over it. For example, the ray-scan function of the line $y = k$ in 2d returns $\sigma = -\text{sign}(\hat{n}_y)$ and $z = \frac{k - \mathbf{o}_y}{\hat{n}_y}$. When supplied with quadratic domain coefficients, or a general domain $f(x) > 0$, the toolbox ray-scans it automatically under the hood. For a general domain, the numerical root-finding works only in a finite interval, and is slower and may introduce small errors. So, a slightly faster and more accurate alternative to the general domain format is to directly construct its ray-scan function by hand.

2.2.3 Standard normal distribution on a ray

In order to integrate over piecewise intervals of z such as fig. 1b, we shall first calculate the semi-definite integral up to some z , then stitch them together over the intervals.

Consider the probability in the angular slice $d\hat{n}$ below some negative z such as z_1 in fig. 1a. Note that the probability of a standard normal beyond some radius is given by the chi distribution. If Ω_d is the total angle in d dimensions (2 in 1d, 2π in 2d, 4π in 3d), and $F_{\chi_d}(x)$ is the cdf of the chi distribution with d degrees of freedom, we have:

$$\Omega_d \int_{-\infty}^{z < 0} (2\pi)^{-\frac{d}{2}} e^{-\frac{z^2}{2}} dz = 1 - F_{\chi_d}(|z|).$$

So the probability in the angular slice $d\hat{n}$ below a negative z is $[1 - F_{\chi_d}(|z|)] \frac{d\hat{n}}{\Omega_d}$. Now, for the probability in the angular slice below a positive z (such as z_2), we need to add two probabilities: that in the finite cone from the origin to the point, which is $F_{\chi_d}(z) \frac{d\hat{n}}{\Omega_d}$, and that in the entire semi-infinite cone on the negative side, which is $\frac{d\hat{n}}{\Omega_d}$, to obtain $[1 + F_{\chi_d}(z)] \frac{d\hat{n}}{\Omega_d}$. Thus, the probability in an angular slice $d\hat{n}$ below a positive or negative z is $[1 + \text{sign}(z)F_{\chi_d}(|z|)] \frac{d\hat{n}}{\Omega_d}$. We normalize this by the total probability in the angular slice, $2 \frac{d\hat{n}}{\Omega_d}$, to define the distribution of the standard normal along a ray: $\Phi_d^{\text{ray}}(z) = [1 + \text{sign}(z)F_{\chi_d}(|z|)] / 2$. Its density is found by differentiating: $\phi_d^{\text{ray}}(z) = f_{\chi_d}(|z|)/2$, so it is simply the chi distribution symmetrically extended to negative numbers. Notice that $\phi_1^{\text{ray}}(z) = \phi(z)$, but in higher dimensions it rises, then falls outward (fig. 1b), due to the opposing effects of the density falling but the volume of the angular slice growing outward. Since Matlab does not yet incorporate the chi distribution, we instead define, in terms of the chi-square distribution, $\Phi_d^{\text{ray}}(z) = [1 + \text{sign}(z)F_{\chi_d^2}(z^2)] / 2$ and $\phi_d^{\text{ray}}(z) = |z|f_{\chi_d^2}(z^2)$.

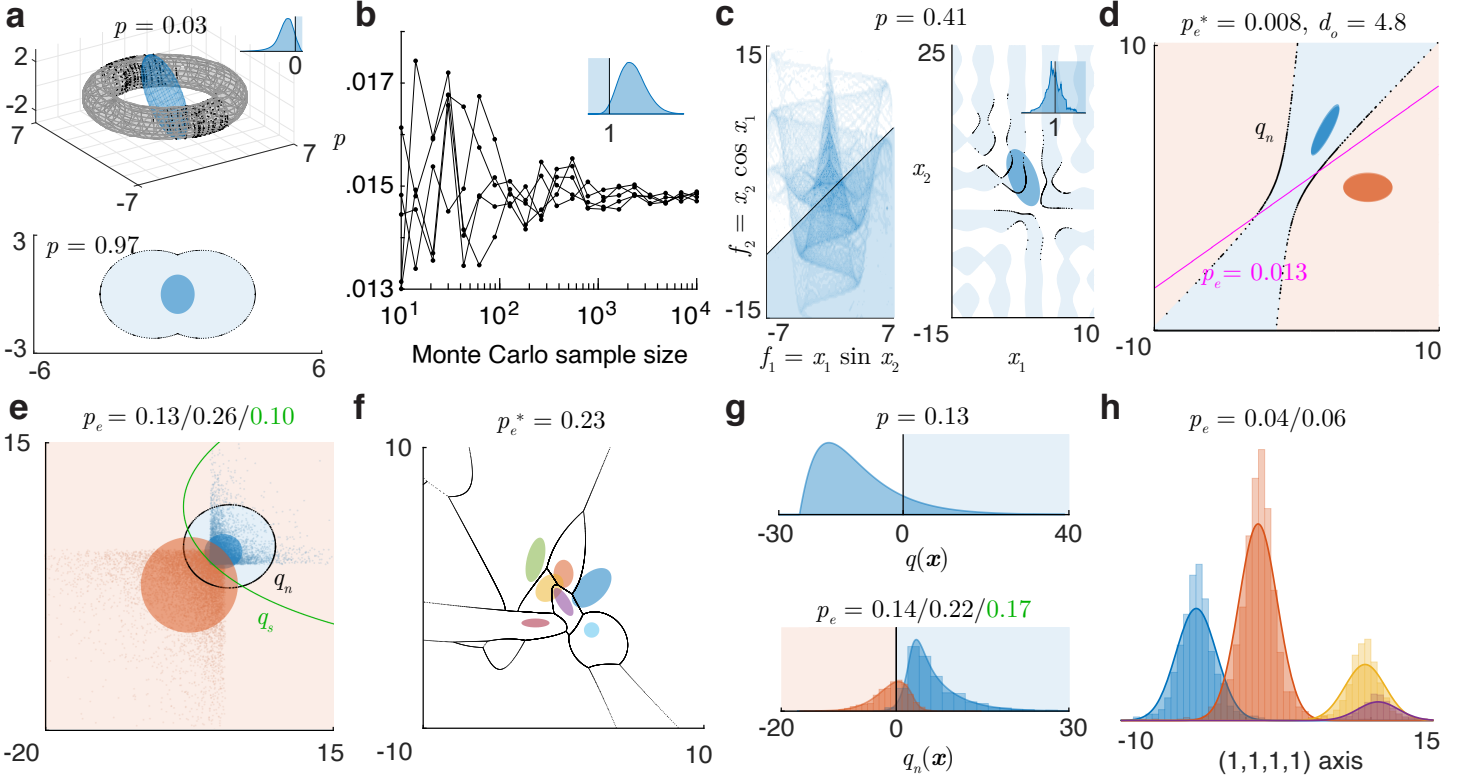


Figure 2: Toolbox outputs for some integration and classification problems. **a.** Top: the probability of a 3d normal (blue shows 1 sd error ellipsoid) in an implicit toroidal domain $f_t(\mathbf{x}) > 0$. Black dots are boundary points within 3 sd scanned by the ray method, across Matlab’s adaptive integration grid over angles. Inset: pdf of $f_t(\mathbf{x})$ and its integrated part (blue overlay). Bottom: integrating a 2d normal (blue error ellipse) in a domain built by the union of two circles. **b.** Monte Carlo estimates of the 4d standard normal probability in a 4d polyhedral domain $f_p(\mathbf{x}) < 1$, across multiple runs, converging with growing sample size. Inset: pdf of $f_p(\mathbf{x})$ and its integrated part. **c.** Left: heat map of joint pdf of two functions of a 2d normal, to be integrated over the implicit domain $f_1 - f_2 > 1$ (overlay). Right: corresponding integral of the normal over the domain $h(\mathbf{x}) = x_1 \sin x_2 - x_2 \cos x_1 > 1$ (blue regions), ‘scanned’ up to 3 sd (black dots). Inset: pdf of $h(\mathbf{x})$ and its integrated part. **d.** Classifying two 2d normals using the optimal boundary q_n (which provides the d_o), and a custom linear boundary. **e.** Classification based on samples (dots) from non-normal distributions. Filled ellipses are error ellipses of fitted normals. q_s is an optimized boundary between the samples. The three error rates are: of the normals with q_n , of the samples with q_n , and of the samples with q_s . **f.** Classifying several 2d normals with arbitrary means and covariances. **g.** Top: 1d projection of a 4d normal integral over a quadratic domain $q(\mathbf{x}) > 0$. Bottom: 1d projection of classifying two 4d normals based on samples, with unequal priors, and unequal outcome values (correctly classifying the blue class is valued 4 times the red, hence the optimal criterion is shifted). Histograms and smooth curves are the projections of the samples and the fitted normals. The sample-optimized boundary q_s cannot be plotted on this q_n axis. **h.** Classification based on four 4d non-normal samples, with different priors and outcome values, projected on the axis along (1,1,1,1). The boundaries cannot be projected to this axis.

2.2.4 Probability in an angular slice

We can now write the total probability in the angular slice of fig. 1 as the sum of terms accounting for the initial sign and each root. Without roots, this probability would be $d\hat{\mathbf{n}}$ times $\frac{2}{\Omega_d} / \frac{1}{\Omega_d} / 0$ accordingly as $\sigma = 1/0/-1$, summarized as $\frac{\sigma(\hat{\mathbf{n}})+1}{\Omega_d}$. To this we add the integral from each root to ∞ , signed according to whether we are entering or exiting the domain at that root:

$$dp(\hat{\mathbf{n}}) = \left[\frac{2}{\Omega_d} - \frac{2\bar{\Phi}_d^{\text{ray}}(z_1)}{\Omega_d} + \frac{2\bar{\Phi}_d^{\text{ray}}(z_2)}{\Omega_d} \right] d\hat{\mathbf{n}}.$$

The sign of the first root term is always opposite to σ , and subsequent signs alternate as we enter and leave the domain. In general

then:

$$dp(\hat{\mathbf{n}}) = \underbrace{\left[\sigma(\hat{\mathbf{n}}) + 1 + 2\sigma(\hat{\mathbf{n}}) \sum_i (-1)^i \bar{\Phi}_d^{\text{ray}}(z_i(\hat{\mathbf{n}})) \right]}_{\alpha(\hat{\mathbf{n}})} \frac{d\hat{\mathbf{n}}}{\Omega_d}$$

Thus, the axial integral is $\frac{\alpha(\hat{\mathbf{n}})}{\Omega_d}$. The total probability $\frac{1}{\Omega_d} \int \alpha(\hat{\mathbf{n}}) d\hat{\mathbf{n}}$ can be computed, for up to 3d, by numerically integrating $\alpha(\hat{\mathbf{n}})$ over a grid of angles spanning half the angular space (since we account for both directions of a ray), using any standard scheme. An adaptive grid can match the shape of the integration boundary (finer grid at angles where the boundary is sharply changing), and also set its fineness to evaluate the integral to a desired absolute or relative precision. Fig. 2a, top, illustrates integrating a trivariate normal with arbitrary covariance in an implicitly-defined toroidal domain $f_t(\mathbf{x}) = a - (b - \sqrt{x_1^2 + x_2^2})^2 - x_3^2 > 0$.

Beyond 3d, we can use Monte Carlo integration over the angles. We draw a sample of \mathbf{z} 's from the standard normal in those dimensions, then $\hat{\mathbf{n}} = \frac{\mathbf{z}}{\|\mathbf{z}\|}$ is a uniform random sample of rays, over which the expectation $\langle \alpha(\hat{\mathbf{n}}) \rangle_{\hat{\mathbf{n}}} / 2$ is the probability estimate. Fig. 2b shows the computation of the 4d standard normal probability in the domain $f_p(\mathbf{x}) = \sum_{i=1}^4 |x_i| < 1$, a 4d extension of a regular octahedron with plane faces meeting at sharp edges.

Since the algorithm already computes the boundary points over its angular integration grid, they may be stored for plotting and inspecting the boundary. Rather than an adaptive integration grid though, boundaries are often best visualized over a uniform grid (uniform array of angles in 2D, or a Fibonacci sphere in 3D⁹), which we can explicitly supply for this purpose.

2.2.5 Set operations on domains

Some applications require more complex integration or classification domains built using set operations (and/or/not) on simpler domains. With general domain formats this is easy, e.g. if $f_A(\mathbf{x}) > 0$ and $f_B(\mathbf{x}) > 0$ define two general domains A and B , then \bar{A} , $A \cap B$, and $A \cup B$ are described by $-f_A(\mathbf{x}) > 0$, $\min(f_A(\mathbf{x}), f_B(\mathbf{x})) > 0$ and $\max(f_A(\mathbf{x}), -f_B(\mathbf{x})) > 0$ respectively. Fig. 2a, bottom, illustrates integrating a 2d normal in a domain built by the union of two circles.

As noted previously, ray-scan domain formats yield slightly faster and more accurate results. So the toolbox provides functions to convert quadratic and general domains to ray-scan format, and functions to use set operations on these to build complex ray-scan domains. For example, when a domain is inverted, only the initial sign of a ray through it flips, and for the intersection of several domains, the initial sign of a ray is the minimum of its individual initial signs, and the roots are found by collecting those roots of each domain where every other domain is positive.

2.2.6 Probabilities of functions of a normal vector

We previously mentioned the equivalent ‘normal probability’ and ‘function probability’ pictures of conceptualizing a normal integral. So far we have mostly used the normal probability notion, seeing scalar functions $f(\mathbf{x})$ as defining integral domains of the normal \mathbf{x} . But in the function probability picture, $f(\mathbf{x})$ is instead seen as a mapping from the multiple variables \mathbf{x} to a single one, which can be considered a decision variable. Hence, integrating the normal in the multi-dimensional domain $f(\mathbf{x}) > 0$ corresponds to integrating the 1d pdf of the decision variable $f(\mathbf{x})$ beyond 0. It is helpful to plot this 1d pdf, especially when there are too many dimensions of \mathbf{x} to visualize the normal probability picture. Conversely, given any scalar function $f(\mathbf{x})$ of a normal, its cdf, $F_f(c) = p(f(\mathbf{x}) < c)$, is computed as the normal probability in the domain $c - f(\mathbf{x}) > 0$. Differentiating this gives us the pdf. (If it is a quadratic function, its generalized chi-square pdf can also be computed by convolving the constituent noncentral chi-square pdf's.) Figs. 2a-c and g show 1d pdf's of functions computed in this way. Also, inverting the function cdf using a numerical root-finding method gives us its inverse cdf (percentage points). Using these we can compute, for example, that if x and y are jointly normal with $\mu_x = 1$, $\mu_y = 2$, $\sigma_x = .1$, $\sigma_y = .2$, and $\rho_{xy} = .8$, then the mean, median and sd of x^y are respectively 1.03, 1 and 0.21.

The probability of a vector (multi-valued) function of the normal, e.g. $\mathbf{f}(\mathbf{x}) = [f_1(\mathbf{x}) \ f_2(\mathbf{x})]$, in some \mathbf{f} -domain (which may also be seen as the joint probability of two scalar functions), is again the normal probability in a corresponding \mathbf{x} -domain. For example, the joint cdf $F_{\mathbf{f}}(c_1, c_2)$ is the function probability in an explicit domain: $p(f_1 < c_1, f_2 < c_2)$, and can be computed as the normal probability in the intersection of the \mathbf{x} -domains $f_1(\mathbf{x}) < c_1$ and $f_2(\mathbf{x}) < c_2$, i.e. the domain $\min(c_1 - f_1(\mathbf{x}), c_2 - f_2(\mathbf{x})) > 0$. Numerically computing $\frac{\partial}{\partial c_1} \frac{\partial}{\partial c_2} F_{\mathbf{f}}(c_1, c_2)$ then gives the joint pdf of the vector function. Fig. 2c, left, is an example of a joint pdf of two functions of a bivariate normal with $\boldsymbol{\mu} = [-2 \ 5]$ and $\boldsymbol{\Sigma} = \begin{bmatrix} 10 & -7 \\ -7 & 10 \end{bmatrix}$, computed in this way.

The probability of such a vector function in an implicit domain, i.e. $p(g(\mathbf{f}) > 0)$, is computed as the normal probability in the implicit domain: $p(h(\mathbf{x}) > 0)$ where $h = g \circ \mathbf{f}$. Fig. 2c illustrates the function probability and normal probability pictures of the implicit integral $p(h = x_1 \sin x_2 - x_2 \cos x_1 > 1)$. The 83rd percentile of this function h (using the inverse cdf) is 4.87.

3 Classifying normal samples

Suppose observations come from several normal distributions with parameters $\boldsymbol{\mu}_i, \boldsymbol{\Sigma}_i$ and priors p_i , and the outcome values (rewards and penalties) of classifying them are represented in a matrix \mathbf{V} : v_{ij} is the value of classifying a sample from i as j .

If the true class is i , selecting i over others provides a relative value gain of $v_i := v_{ii} - \sum_{j \neq i} v_{ij}$. Given a sample \mathbf{x} , the expected value gain of deciding i is therefore $\langle v(i|\mathbf{x}) \rangle = p(i|\mathbf{x})v_i = p(\mathbf{x}|i)p_iv_i$. The Bayes-optimal decision is to assign each sample to the class that maximizes this expected value gain, or its log:

$$\ln \langle v(i|\mathbf{x}) \rangle = -\frac{1}{2}(\mathbf{x} - \boldsymbol{\mu}_i)' \boldsymbol{\Sigma}_i^{-1}(\mathbf{x} - \boldsymbol{\mu}_i) + \ln \frac{p_i v_i}{\sqrt{|\boldsymbol{\Sigma}_i|} (2\pi)^d}.$$

When the outcome value is simply the correctness of classification, $\mathbf{V} = \mathbf{1}$ (so each $v_i = 1$), then this quantity is the log posterior, $\ln p(i|\mathbf{x})$.

3.1 Two normals

If there are only two normal classes a and b , the Bayes-optimal decision is to pick a if

$$\begin{aligned} \ln \frac{\langle v(a|\mathbf{x}) \rangle}{\langle v(b|\mathbf{x}) \rangle} &= q_n(\mathbf{x}) = \mathbf{x}' \mathbf{Q}_2 \mathbf{x} + \mathbf{q}_1' \mathbf{x} + q_0 > 0, \text{ where:} \\ \mathbf{Q}_2 &= \frac{1}{2} (\boldsymbol{\Sigma}_b^{-1} - \boldsymbol{\Sigma}_a^{-1}), \\ \mathbf{q}_1 &= \boldsymbol{\Sigma}_a^{-1} \boldsymbol{\mu}_a - \boldsymbol{\Sigma}_b^{-1} \boldsymbol{\mu}_b, \\ q_0 &= \frac{1}{2} \left(\boldsymbol{\mu}_b' \boldsymbol{\Sigma}_b^{-1} \boldsymbol{\mu}_b - \boldsymbol{\mu}_a' \boldsymbol{\Sigma}_a^{-1} \boldsymbol{\mu}_a + \ln \frac{|\boldsymbol{\Sigma}_b|}{|\boldsymbol{\Sigma}_a|} \right) + \ln \frac{p_a v_a}{p_b v_b}. \end{aligned} \quad (3)$$

This quadratic $q_n(\mathbf{x})$ is the Bayes classifier, or the Bayes decision variable to classify two normals (when $\mathbf{V} = \mathbf{1}$, it is the log posterior ratio). The classification outcome probabilities (error

rates) of different types, i.e. true and false positives and negatives, are the probabilities of the normals on either side of this quadratic boundary, which can be computed using the methods we discussed. The overall Bayes error p_e is the prior-weighted sum of the error rates of each normal.

For 1d normals (μ_a, σ_a) and (μ_b, σ_b) with $\sigma_a > \sigma_b$, we can calculate, using the generalized chi-square method, that the optimal classification errors are:

$$p_e(a) = F_{\chi^2_{1, \sigma_a \lambda}}(\sigma_b c), \quad p_e(b) = \bar{F}_{\chi^2_{1, \sigma_b \lambda}}(\sigma_a c), \quad (4)$$

$$\text{where } \lambda = \left(\frac{\mu_a - \mu_b}{\sigma_a^2 - \sigma_b^2} \right)^2, \quad c = \lambda + \frac{2 \ln \frac{\sigma_a}{\sigma_b}}{\sigma_a^2 - \sigma_b^2},$$

and the Bayes error p_e^* is their average.

3.1.1 Discriminability index

The discriminability between two equal-variance normals is $d' = |\mu_a - \mu_b|/\sigma$ in 1d, and in multiple dimensions it is the Mahalanobis distance: $d' = \sqrt{(\mu_a - \mu_b)' \Sigma^{-1} (\mu_a - \mu_b)} = \|\mathbf{S}^{-1}(\mu_a - \mu_b)\| = \|\mu_a - \mu_b\|/\sigma_{\hat{\mu}}$, where $\sigma_{\hat{\mu}} = 1/\|\mathbf{S}^{-1}\hat{\mu}\|$ is the 1d slice of the sd along the axis $\hat{\mu}$ through the means, i.e. the d' is equal to the 1d d' along the slice through the means. For unequal variances, there exist several contending indices.^{10–12} A common one is $d_a = |\mu_a - \mu_b|/\sigma_{\text{rms}}$, extended to general dimensions as the Mahalanobis distance using the pooled covariance, i.e. with $\mathbf{S}_{\text{rms}} = [(\Sigma_a + \Sigma_b)/2]^{\frac{1}{2}}$ as the common sd.¹³ Another index is $d'_e = |\mu_a - \mu_b|/\sigma_{\text{avg}}$,¹² which we here extend to general dimensions using $\mathbf{S}_{\text{avg}} = (\mathbf{S}_a + \mathbf{S}_b)/2$.

These unequal-variance indices are simple approximations that do not measure the exact overlap of the two distributions. With our methods we can compute this overlap for normal distributions, which is the Bayes error rate p_e^* (with equal priors, $\mathbf{V} = \mathbf{1}$, and the Bayes classifier), e.g. eq. 4 for 1d. So we define a new index that is twice the z -score of this optimal accuracy, i.e. the separation between two unit variance normals that have this overlap:

$$d_o = 2Z(1 - p_e^*) = 2Z(\text{optimal accuracy})$$

where the subscript o indicates *optimal* or *overlap*. This index extends to all cases as a smooth function of the layout and shapes of the normals, and reduces to d' for equal covariance.

Discriminability indices are frequently estimated from ROC curves, which track the performance of a single shifting criterion between two normals. d_o uses both criteria when variances are unequal, but can still be estimated from an ROC curve. Assume that two 1d normals are at 0 and 1 with sd's $s\sigma$ and σ . From the ROC curve, we can calculate d_a or d'_e and the ratio s . Then we back out $\sigma = \frac{1}{d_a} \sqrt{\frac{2}{s^2+1}}$ or $\frac{2}{d'_e(s+1)}$, then use our method to compute d_o of the normals with these estimated normal parameters.

In fig. 3a, we compare d_o with d_a and d'_e for different mean-separations and sd ratios of two normals, in 1d and 3d. We first take two 1d normals and increase their discriminability by equally shrinking their sd's while maintaining their ratio $\sigma_a/\sigma_b = s$, i.e. effectively separating the means. We repeat this by starting with two 3d normals with different sd matrices, one of them scaled by different values s each time, then shrink them equally.

Extending previous findings,¹² we see that $d_a \leq d'_e \leq d_o$. Thus, d_a and d'_e underestimate the optimal discriminability. The

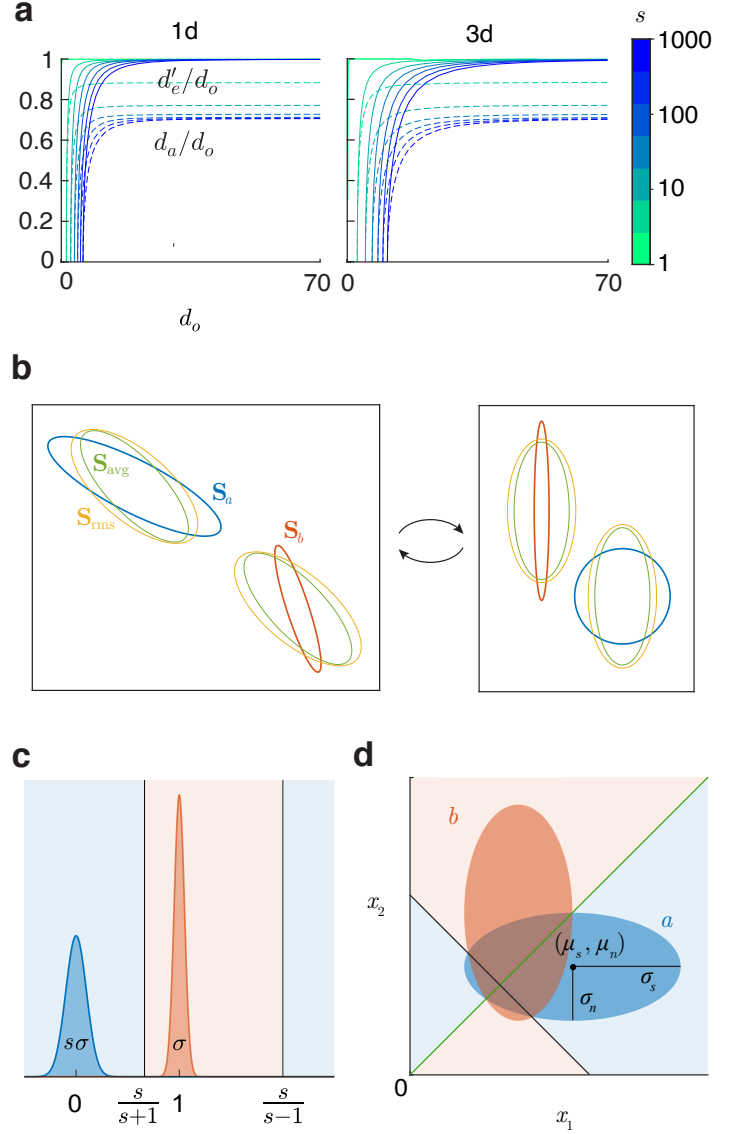


Figure 3: Comparing discriminability indices. **a.** Plots of existing indices d_a and d'_e as fractions of our optimal index d_o , with increasing separation between two normals in 1d and 3d, for different ratios s of their sd's. **b.** Left : two normals with 1 sd error ellipses corresponding to their sd matrices \mathbf{S}_a and \mathbf{S}_b , and their average and rms sd matrices. Right: the space has been linearly transformed, so that a is now standard normal, and b is aligned with the coordinate axes. **c.** Discriminating two highly-separated 1d normals. **d.** A two-interval forced-choice discrimination task between signal and noise distributions $N(\mu_s, \sigma_s)$ and $N(\mu_n, \sigma_n)$.

worst case is when the means are equal, so $d_a = d'_e = 0$, but d_o is positive, since unequal variances still provide discriminability.

Now consider the opposite end, where large mean-separation has a much greater effect on discriminability than sd ratios. Even here, the underestimate by d_a persists (fig. 3a), and worsens as the sd's become more unequal, reaching nearly 30% in the worst case. d'_e is a better estimate throughout, and equals d_o at large separation. So, when two normals are too far apart to compute their overlap (see performance section), the toolbox returns d'_e instead.

We can prove some of these results for all dimensions and cases.

In 1d, $d_a \leq d'_e$ simply because $\sigma_{\text{avg}} \leq \sigma_{\text{rms}}$, and at the limit of highly unequal sd's, $\sigma_{\text{avg}}/\sigma_{\text{rms}} \rightarrow 1/\sqrt{2}$, so $d_a \rightarrow d'_e/\sqrt{2}$, which is the 30% underestimate. In higher dimensions, we can show analogous results using fig. 3b as an example. The left figure shows two normals with error ellipses corresponding to their sd's, and their average and rms sd's. Now we make two linear transformations of the space: first we standardize normal a , then we diagonalize normal b (i.e. a rotation that aligns the axes of error ellipse b with the coordinate axes). In this space (right figure), $\mathbf{S}_a = \mathbf{I}$, \mathbf{S}_b is diagonal, and the axes of \mathbf{S}_{avg} and \mathbf{S}_{rms} are the average and rms of the corresponding axes of \mathbf{S}_a and \mathbf{S}_b . \mathbf{S}_{rms} is hence bigger than \mathbf{S}_{avg} , so has larger overlap at the same separation, so $d_a \leq d'_e$. The ratio of d_a and d'_e is $\|\mathbf{S}_{\text{rms}}^{-1}\hat{\boldsymbol{\mu}}\|/\|\mathbf{S}_{\text{avg}}^{-1}\hat{\boldsymbol{\mu}}\|$, the ratio of the 1d slices of the average and rms sd's along the axis through the means. When these are highly unequal, we again have $d_a \rightarrow d'_e/\sqrt{2}$ in general dimensions.

We can also show that at large separation, $d'_e = d_o$. Consider normals at 0 and 1 with sd's $s\sigma$ and σ (fig. 3c). At large separation ($\sigma \rightarrow 0$), the boundary points are $\frac{s}{s \pm 1}$. The right boundary is $\frac{1}{\sigma(s-1)}$ sd's from each normal, so it adds as much accuracy for the left normal as it subtracts for the right, so we can ignore it. The inner boundary is $\frac{1}{\sigma(s+1)}$ sd's from each normal. The overlap here thus corresponds to $d_o = \frac{2}{\sigma(s+1)} = d'_e$. For far-apart normals in higher dimensions, we first squeeze their separation down to 1. At this limit, the boundary will be flat and perpendicular to the axis connecting the means, so we can simply consider this axis, and arrive at the same 1d case above.

Given that d'_e is the better approximation to the optimal discriminability d_o , why is d_a used so often? Simpson and Fitter¹² argued that d_a is the best index, because it is the detectability in a two-interval task (where two stimuli x_1 and x_2 come from the signal and noise distributions $N(\mu_s, \sigma_s)$ and $N(\mu_n, \sigma_n)$ respectively, or vice versa), using the criterion $x_1 > x_2$. But note that this task is to actually classify (x_1, x_2) between two 2d normals: a with mean $\boldsymbol{\mu}_a = (\mu_s, \mu_n)$ and sd $\mathbf{S}_a = \text{diag}(\sigma_s, \sigma_n)$, and its mirror b (fig. 3d). Using $x_1 > x_2$ is to use only the green boundary, which makes it a 1d classification and loses information. When $\sigma_s \neq \sigma_n$, the optimal boundary also includes a perpendicular line, and the optimal error rate can be calculated to be $p_e^* = F_{\tilde{\chi}_{w, \mathbf{k}, \boldsymbol{\lambda}, 0, 0}^2}(0)$, where

$$\mathbf{w} = [\sigma_s^2 \quad -\sigma_n^2], \mathbf{k} = [1 \quad 1], \boldsymbol{\lambda} = \frac{\mu_s - \mu_n}{\sigma_s^2 - \sigma_n^2} [\sigma_s^2 \quad \sigma_n^2],$$

and $d_o(a, b) = 2Z(1 - p_e^*)$ is the exact discriminability. We can also calculate that $d'_e(a, b) = \sqrt{2}d'_e(s, n)$, which is still a better approximation than $d_a(a, b) = \sqrt{2}d_a(s, n)$.

Two other common indices are worth comparing against d_o . d_{gm} , the approximation using the geometric mean of the sd's, is less than d_o at small separation, but greater at large separation. Another measure is $Z(\text{hit rate}) - Z(\text{false alarm rate}) = z_{tp} + z_{tn}$ (sum of z -scores of the true positive and negative rates), usually using a single boundary, which makes it sub-optimal for unequal-variance normal distributions. Even if z_{tp} and z_{tn} are obtained using the optimal boundary in any dimensions, $d_o = 2\Phi^{-1}[(\Phi(z_{tp}) + \Phi(z_{tn}))/2] \leq z_{tp} + z_{tn}$ (since the function $\Phi(z)$ is concave downwards for positive numbers). So this measure is larger than d_o , and converges to d_o at large separation.

d_o thus measures the Bayes-optimal discriminability between normals in all cases, including two-interval tasks, especially when means are closer and variances are unequal, and d'_e is always a better approximation than d_a .

3.1.2 Custom classifiers

Sometimes, instead of the optimal classifier, we need to test and compare sub-optimal classifiers, e.g. one that ignores a cue, or some cue covariances, or a simple linear classifier. For this reason, the toolbox allows the user to extract the optimal boundary, change it, and explicitly supply some custom boundary to use in place of the optimal boundary. Fig. 2d compares the classification of two bivariate normals using the optimal boundary (which provides the d_o), vs. using a hand-supplied linear boundary. Just as with integration, one can supply custom classification domains in quadratic, ray-scan or implicit form, and use set operations on them.

3.2 Classifying using data

If instead of normal parameters, we have labelled data as input, we can estimate the parameters. The maximum-likelihood estimates of the means, covariances and priors of normals are simply the sample means, covariances and relative frequencies. With these estimated parameters we can compute the optimal classifier $q_n(\mathbf{x})$ and the error matrix. We can further calculate another quadratic boundary $q_s(\mathbf{x})$ to separate the given samples even better: we start with $q_n(\mathbf{x})$, then optimize its $(d+1)(d+2)/2$ independent parameters to maximize the classification outcome value of the given samples. This is especially helpful with non-normal data, where the optimal boundary between estimated normals is not the best classifier. This optimization then improves classification while still staying within the smooth quadratic family and preventing overfitting. Fig. 2e shows classification based on labelled non-normal samples.

If, along with labelled samples, we supply a custom quadratic classifier, the toolbox instead optimizes this for the sample. This is useful, say, in the following case: suppose we have already computed the optimal classifier for samples in some feature space. Now if we augment the data with additional features, we may start from the existing classifier (with its coefficients augmented with zeros in the new dimensions) to find the optimal classifier in the larger feature space.

3.3 Multiple normals

The optimal decision boundary between two normals is a quadratic, hence classification error rates can be computed using the generalized chi-square method or the ray-scan method. When classifying amongst more than two normals, the decision region for each normal is the intersection of its quadratic decision regions $q_n^i(\mathbf{x}) > 0$ with all the other normals i , and may be written as:

$$f(\mathbf{x}) = \min_i q_n^i(\mathbf{x}) > 0.$$

This is not a quadratic, so only the ray-scan method can compute the error rates here, by using the intersection operation on the

domains as described before. Fig. 2f shows the classification of several normals with arbitrary means and covariances.

3.4 Combining and reducing dimensions

Reducing a many-dimensional integration problem to fewer dimensions allows visualization. Projecting a normal \mathbf{x} to an axis, or mapping \mathbf{x} to its Mahalanobis distance (related to its log probability), are ways to project the distribution to 1d. However, in an integration problem of finding $p(f(\mathbf{x}) > 0)$, these will not uniquely map the integration domain boundary $f(\mathbf{x}) = 0$. Instead, in light of our previous discussion, we can map $\mathbf{x} \rightarrow f(\mathbf{x})$, which maps the problem to the 1d function probability picture of integrating the pdf of $f(\mathbf{x})$ above 0. For quadratic integrations beyond 3d, the toolbox plots the pdf of this projection $q(\mathbf{x})$ (fig. 2g, top), which is a quadratic function of a normal, so distributed as a generalized chi-square.

Similarly, in a classification or estimation problem, we often want to optimally combine the available cues into one.¹⁴ For a binary classification with a classifier $f(\mathbf{x}) = 0$, we can map $\mathbf{x} \rightarrow f(\mathbf{x})$, which combines the cues into a single decision variable, and projects the problem to a 1d classification on its axis with the boundary at 0, with all classification errors preserved. For the default optimal classification, mapping to the Bayes decision variable $\mathbf{x} \rightarrow q_n(\mathbf{x})$ is the optimal quadratic combination of the cues. The toolbox shows this projection, which is distributed as a generalized chi-square (fig. 2g, bottom). For a many-dimensional problem, we can define a decision variable on a subset of dimensions and so combine them into one, then combine those further etc, as we shall demonstrate later. With multiple classes, there is no single decision variable to project to, but the toolbox plots the projection along any chosen axis. Fig. 2h shows the classification using normal fits to samples from four 4d t distributions, projected onto the axis along (1,1,1,1).

3.5 Testing a normal model for classification

The results developed here are for normal distributions. But even when the variables in a classification problem are not exactly normal (i.e. have an empirical or some other known theoretical distribution), we can still use these results if we check that normals are an adequate model, i.e. an equivalence test. One test is to project the distributions to one dimension, either by mapping to a quadratic form (fig. 2g), or to an axis (fig. 2h), where we can visually compare the projections of the observed distributions and those of their fitted normals.

We could further explicitly test the normality of the variables with measures like negentropy, but this is often stricter than needed. For example, if the final test of the normal model is against outcomes of a limited-trials classification experiment, it suffices to check that it predicts similar enough performance as the true distributions, with the given number of trials. For any classification boundary, we can calculate outcome rates, e.g. $p(a|a)$ for a hit, determined from the true distributions, vs. from the normal approximations. The count of hits in a task is binomial with parameters equal to the number of a trials and $p(a|a)$, so we can compare its count distribution between the true and the normal model.

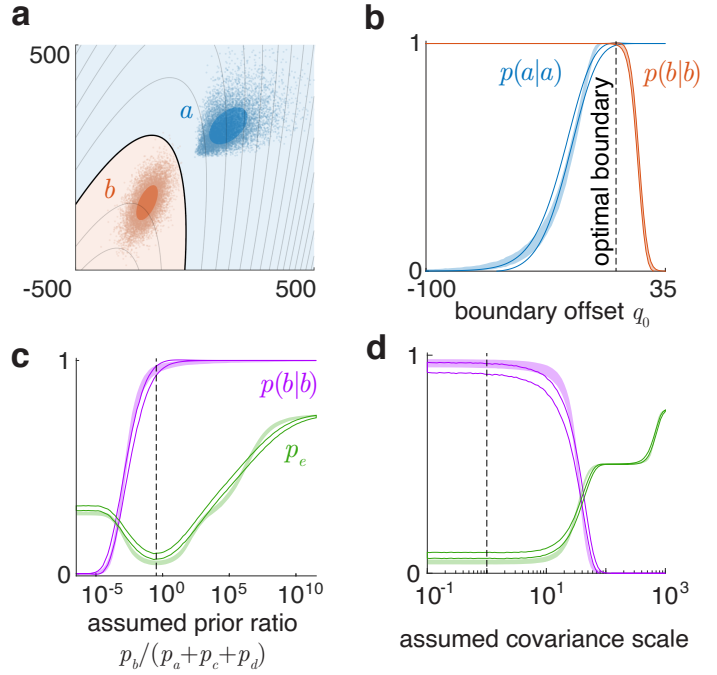


Figure 4: Testing normal approximations for classification. **a.** Classifying two empirical distributions (a is not normal). Gray curves are a family of suboptimal boundaries. **b.** Mean \pm sd of hits and correct rejections observed (color fills) vs. predicted by the normal model (outlines), along this family of boundaries. **c.** Similar bands for class b hits and overall error, for the 4d 4-class problem of fig. 2h, across boundaries assuming different priors p_b , and **d.** across boundaries assuming different covariance scales (d 's).

If the classes are well-separated (e.g. for ideal observers), the optimal boundary provides near-perfect accuracy on both the true and the normal distributions, so the comparison yields no insight. To make the test more informative, we repeat it as we sweep the boundary across the space into regions of error, to show decisively if the normal model still stands. This is similar to how the decision criterion between two 1d distributions is swept across to create an ROC curve that characterizes the classification more richly than a single boundary. In multiple dimensions, there is more than a unique way to sweep the boundary. We pick two common suboptimal boundary families. The first corresponds to a model or subject being biased towards one type of error or another, i.e. a change in the assumed ratio of priors or outcome values, reflecting in a shifted offset q_0 of the boundary (eq. 3). The second kind is the observer having an internal discriminability that is different from the true (external) one (e.g. due to blurring by internal noise), so adopting a boundary corresponding to covariance matrices that are scaled (by s , say), which again shifts q_0 , by $\frac{s-1}{2} \ln \frac{|\Sigma_b|}{|\Sigma_a|}$. Thus, with two classes, both kinds of suboptimal boundaries are described by varying q_0 .

Fig. 4a shows the classification of two empirical distributions, where a is not normal, and gray curves show this family of boundaries. Fig. 4b shows the mean \pm sd bands of error rates from applying these boundaries on samples of 100 trials (typical of a psychophysics experiment) from each true distribution, vs. the normal approximations. They exactly coincide for $p(b|b)$, but deviate for $p(a|a)$, correctly reflecting that b is normal but a is not.

The investigator can judge if this deviation is still small enough for their purpose.

Fig. 4c shows similar tests for the 4d 4-class problem of fig. 2h, with priors now equal. The family of boundaries corresponds to varying the assumed prior p_b . We may look at any of the 16 error rates here, e.g. $p(b|b)$, and also the overall error p_e . With multiple classes, the numbers of different outcomes for trials of a class are multinomially distributed, so that the number of its wrong outcomes is again binomially distributed. p_e is the prior-weighted sum of these, so we can calculate its mean and sd predicted by the observed vs. the normal distributions. Fig. 4d shows the test across boundaries corresponding to all covariance matrices scaled by a factor, changing the d' between the classes.

Some other notable suboptimal boundaries to consider for this test are ones that correspond to additive independent noise to the cues (which changes only their variances but not their covariances), ones that ignore certain cues or cue covariances, or simple flat boundaries. As seen here, even for many-dimensional distributions that cannot be visualized, these tests can be performed to reveal some of their structure, and to show which specific outcomes deviate from normal prediction for which boundaries.

When the problem variables have a known non-normal theoretical distribution, the best normal model is the one that matches its mean and covariance, and these tests can be performed by theoretically calculating or bootstrap sampling the error rate distributions induced by the known true distributions.

4 Matlab toolbox functions

For an integration problem, the toolbox provides a function that inputs the normal parameters and the integration domain (as quadratic coefficients or a ray-scan or implicit function), and outputs the integral and its complement, the boundary points computed, and a plot of the normal probability or function probability picture. The function for a classification problem inputs normal parameters, priors, outcome values and an optional classification boundary, and outputs the boundary q_n and points on it, the error matrix and d_o of the normals with q_n , and also d_a and d'_e , and produces a normal probability or function probability plot. With sample input, it additionally returns q_s and points on it, error matrices and d_o values corresponding to classification accuracies of the samples using q_n and q_s , and the mapped decision variables $q_n(\mathbf{x})$ and $q_s(\mathbf{x})$ from the samples. The toolbox also provides functions to compute pdf's, cdf's and inverse cdf's of functions of normals.

Each problem discussed in this paper (examples of fig. 2, tests of figs. 3, 4 and 5, and research applications in fig. 6) is available as an interactive demo in the 'getting started' live script of the toolbox, and can be easily adapted to other problems.

5 Performance benchmarks

A variety of techniques are built into the algorithms to preserve accuracy, such as holding tiny and large summands separate to prevent rounding, using symbolic instead of numerical calculations, and using accurate tail probabilities. We first test for accuracy against known ground truth at the limit of high d' where it

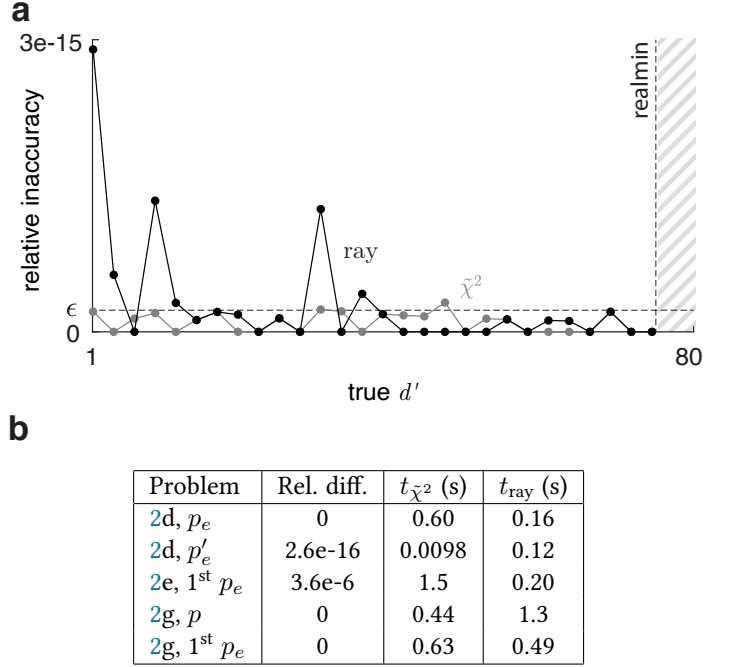


Figure 5: Performance benchmarks of the two algorithms. **a.** Relative inaccuracies in d' estimates by the two methods against known ground truth, with increasing separation. ϵ is machine epsilon. The largest computable $d' \approx 75$, corresponding to the smallest error representable in double precision ('realmin'). **b.** For the quadratic-boundary problems of fig. 2, relative differences in the outputs of the two methods, and their computation times for 1% precision.

is most challenging (which occurs for computational models and ideal observers with high discriminability). We take two 3d normals with the same covariance matrix, so that the true d' is simply their Mahalanobis distance. We increase their separation, while computing the optimal error with both methods at maximum precision, then a d_o from it. Fig. 5a shows the relative inaccuracies $|d_o - d'|/d'$ as true d' increases. Inaccuracies in both methods are equally negligible, do not grow with increasing separation, and are in fact of the order of the double-precision machine epsilon ϵ , demonstrating that neither algorithm contains any significant error source besides machine imprecision (however, Matlab's native integration methods sometimes silently fail to reach the desired precision). $d' \approx 75$ corresponds to the smallest error rate p_e representable in double-precision ('realmin' = 2e-308), beyond which both methods return $p_e = 0$ and $d_o = \infty$, so the toolbox returns d'_e instead.

Second, for problems with no ground truth but quadratic boundaries, we can check the two methods for agreement. For such problems in fig. 2, we compute the values (integrals or error rates) v_{χ^2} and v_{ray} up to practicable precisions Δv_{χ^2} and Δv_{ray} . If they are equal within error, i.e. $|v_{\chi^2} - v_{\text{ray}}| < \Delta v_{\chi^2} + \Delta v_{\text{ray}}$, we call their relative difference as 0, otherwise it is $|v_{\chi^2} - v_{\text{ray}}| / [(v_{\chi^2} + v_{\text{ray}}) / 2]$. Table 5b lists these, along with the times to compute each to 1% precision. The methods produce nearly identical values at comparable speeds.

6 Applications in visual detection

We demonstrate the use of these methods in visual detection tasks with multiple cues with different variances and correlations.

6.1 Detecting targets in natural scenes

We have applied this method in a study to measure how humans compare against a nearly ideal observer in detecting occluding targets against natural scene backgrounds in a variety of conditions.¹⁵ We placed a target on a random subset of natural images, then blurred and downsampled them to mimic the effect of the early visual system (fig. 6a). We sought to measure how well the targets on these degraded images can be detected using three cues: related to the luminance in the target region, the target pattern, and the target boundary. We computed these cues on the set of images. They form two approximately trivariate normal distributions for the target present vs. absent categories. We then computed the decision boundary, error rate and d_o against varying conditions. Fig. 6b shows the result for one condition, with a hyperboloidal boundary. These error rates and d_o 's can then be compared across conditions.

6.2 Detecting camouflage

We also applied this method in a study measuring performance in detecting camouflaged objects.¹⁶ The major source of information for detecting the object (e.g., fig. 6c) is its edge, which we compute at scales of 2px, 4px and 8px. We extract two scalar features from the edge at each scale: the edge power captures its overall prominence, and the edge spectrum characterizes how this prominence is distributed along the boundary. We thus have 6 total features. Fig. 6d shows the classification of these images using these 6 features. We see from this projection that the a distribution is quite normal, whereas b is nearly so. Consistently, in a normality test for classification with 100 trials, fig. 6e, $p(b|b)$ deviates marginally from its normal prediction, but cannot be told apart much with this number of trials, so we accept the normal approximation here. Fig. 6f shows the classification using only the features at the 2px scale. We use our dimension reduction technique to combine these two cues into one: $\mathbf{x} \rightarrow q_s(\mathbf{x})$, which we call simply the edge cue. Classifying with a 0 criterion on this, fig. 6g, is the same as the 2d classification of fig. 6f, and preserves the errors. We do the same merging at 4px and 8px, thus mapping 6 features to 3. Fig. 6h shows the classification using these 3 combined cues. Due to the information in the two added scales, the classification has improved. The total number of classifier parameters used in this sequential classification is 28 (6 for each of the three 2d classifiers, then 10 when combining them in 3d). The classifier in full 6d has 28 parameters as well, yet is better since it can simultaneously optimize them all. Even so, merging features allows one to combine them in groups and sequences according to the problem structure, and visualize the lower-dimensional spaces.

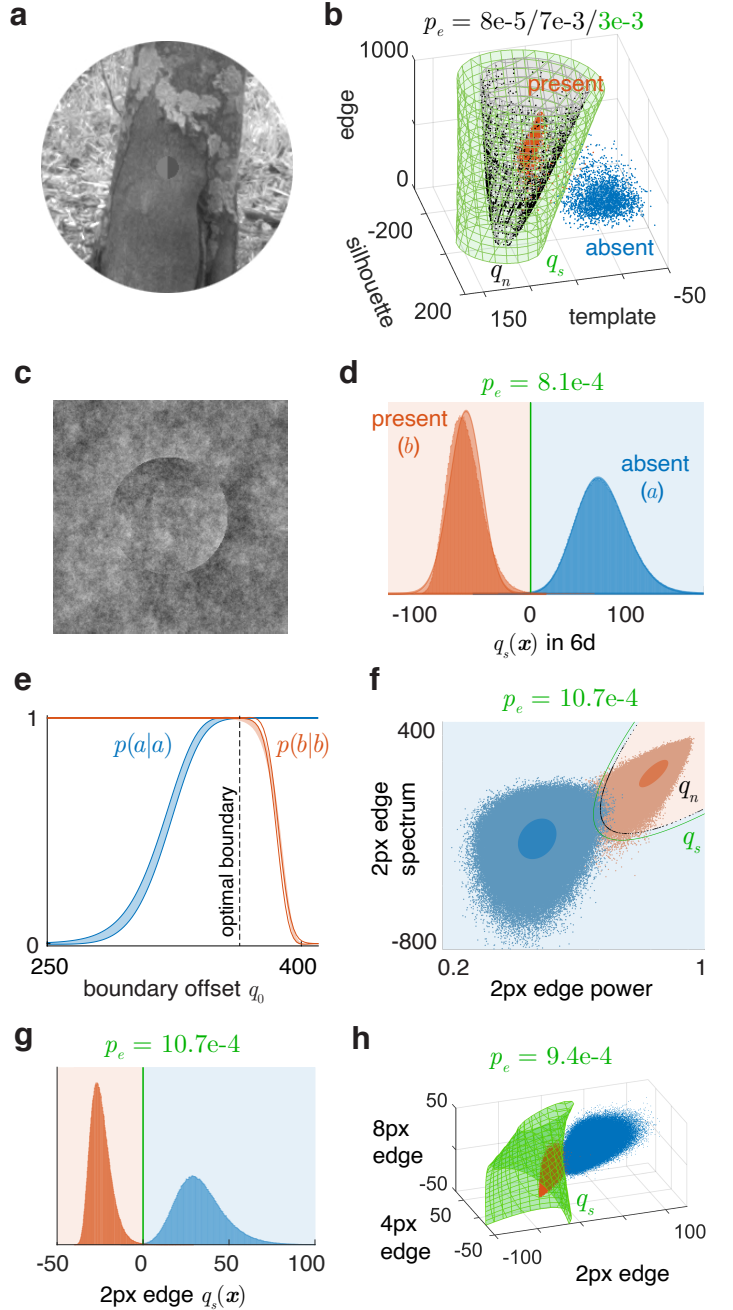


Figure 6: Applying the method and toolbox to visual target detection studies. **a.** Example image of a target on a natural background. **b.** Classification of images with the target present or absent, in the space of three cues. Black dots are the boundary points computed for integration. **c.** Example image for camouflage detection. **d.** Classifying these using 6 cues, combined to 1 using the sample-optimized quadratic. **e.** Bootstrap mean \pm sd of hit and correct rejection fractions from applying a family of offset boundaries on 100 samples of the true 6d cue distributions (color fills), vs. their normal approximations (outlines). **f.** Classifying with only two cues computed at 2px. **g.** Combining the two cues of plot f into one using the sample-optimized quadratic. **h.** Classifying with such combined cues at 3 scales.

7 Conclusions

We begin this paper by describing how to integrate any multivariate normal distribution in a quadratic domain, then present our method and open-source software to integrate in any domain, using examples from the software throughout. We explain how this is synonymous with computing the cdf's of quadratic and arbitrary functions of normal vectors, using which we can then compute their pdf's and inverse cdf's as well.

We then describe how to compute, given the parameters of multiple multinormals or labelled data from them, the expected error rates of classifying amongst them, using optimal or sub-optimal classifiers. We describe how our methods let us compute the optimal discriminability index d_o between two normals. We show that the common approximate indices d_a and d'_e underestimate this optimal discriminability, and that contrary to common use, d'_e is always a better estimate than d_a , even for two-interval tasks.

We next describe methods to merge and reduce dimensions for normal integration and classification problems without losing information. We present tests for how reliably all the above methods, which assume normal distributions, can be used on given data. We follow this by demonstrating the speed and accuracy of the method and software on different problems.

Finally, we illustrate all of the above methods on two visual detection research projects from our laboratory.

8 Acknowledgements

We are thankful to Dr. Johannes Burge (University of Pennsylvania), Dr. R Calen Walshe (University of Texas at Austin) and Kristoffer Frey (MIT) for helpful discussions, feedback and improvements in the method and code. This work was supported by NIH grants EY11747 and EY024662.

References

- 1 Andrew Ng. Generative learning algorithms. *CS229 Lecture notes*, IV, 2019.
- 2 David Marvin Green, John A Swets, et al. *Signal detection theory and psychophysics*, volume 1. Wiley New York, 1966.
- 3 Richard O Duda, Peter E Hart, and David G Stork. *Pattern classification*. John Wiley & Sons, 2012.
- 4 Harold Ruben. Probability content of regions under spherical normal distributions, i. *The Annals of Mathematical Statistics*, 31(3):598–618, 1960.
- 5 Alan Genz and Frank Bretz. *Computation of multivariate normal and t probabilities*, volume 195. Springer Science & Business Media, 2009.
- 6 Harold Ruben. Probability content of regions under spherical normal distributions, iv: The distribution of homogeneous and non-homogeneous quadratic functions of normal variables. *The Annals of Mathematical Statistics*, 33(2):542–570, 1962.
- 7 Robert B Davies. Numerical inversion of a characteristic function. *Biometrika*, 60(2):415–417, 1973.
- 8 Lloyd N Trefethen. *Approximation theory and approximation practice*, volume 164. Siam, 2019.
- 9 Edward B Saff and A BJ Kuijlaars. Distributing many points on a sphere. *The mathematical intelligencer*, 19(1):5–11, 1997.
- 10 Thomas D Wickens. *Elementary signal detection theory*. Oxford University Press, USA, 2002.
- 11 RL Chaddha and LF Marcus. An empirical comparison of distance statistics for populations with unequal covariance matrices. *Biometrics*, pages 683–694, 1968.
- 12 Adrian J Simpson and Mike J Fitter. What is the best index of detectability? *Psychological Bulletin*, 80(6):481, 1973.
- 13 SA Paranjpe and AP Gore. Selecting variables for discrimination when covariance matrices are unequal. *Statistics & probability letters*, 21(5):417–419, 1994.
- 14 Ipek Oruç, Laurence T Maloney, and Michael S Landy. Weighted linear cue combination with possibly correlated error. *Vision research*, 43(23):2451–2468, 2003.
- 15 R Calen Walshe and Wilson S Geisler. Detection of occluding targets in natural backgrounds. *Journal of Vision*, 20(13):14, 2020.
- 16 Abhranil Das and Wilson Geisler. Understanding camouflage detection. *Journal of Vision*, 18(10):549, 2018.